JOURNAL OF MATERIALS SCIENCE 11 (1976) 317–327

Deformation mechanism maps for ceramics

TERENCE G. LANGDON, FARGHALLI A. MOHAMED
Department of Materials Science, University of Southern California, Los Angeles, California, USA

Deformation mechanism maps may be constructed for either a constant grain size or a constant temperature. A simple method is described for constructing maps at constant temperature, and maps are presented for two representative oxides, a carbide, and three alkali halides. A method is also described for superimposing a set of similar deformation mechanism maps.

1. Introduction

Polycrystalline materials may deform by a number of different deformation mechanisms, and the dominant process under any selected testing conditions depends critically on external parameters, such as temperature and stress, and various structural features, such as grain size and purity. For simple systems, such as pure metals, several of the deformation mechanisms are understood reasonably well, and there is often good agreement between theoretical predictions and experimental results.

Weertman [1, 2] first suggested the possibility of using this information to construct a "creep diagram" (now generally referred to as a "deformation mechanism map") in which the normalized stress, σ/G, is plotted as a function of the homologous temperature, T/T_m, at a constant value of the specimen grain size, where σ is the applied stress, G is the shear modulus, T is the absolute temperature, and T_m is the melting point of the material in degrees Kelvin. In the original form of this diagram, four different mechanisms were considered: high temperature (or Andrade) creep, low temperature (or logarithmic) creep, anelastic (or recoverable) creep, and Nabarro–Herring diffusional creep. By examining the form of the constitutive equations describing each of these four processes, and assuming that the mechanisms operated independently so that the strain-rates were additive, the diagram was then divided into four fields so that each mechanism was dominant in one area of stress–temperature space.

The original diagram described by Weertman [1, 2] was only developed schematically, but the concept was of major significance since it provided the opportunity of presenting a compendium of mechanical information in a simple, useful, and highly visual form. As a result, much attention has been devoted recently to the development of deformation mechanism maps for specific materials.

Although most of the published work in this area relates to metals, some maps are now available for ceramic materials. The purpose of this paper is, therefore, three-fold: (1) to briefly review the maps developed to date for non-metallic systems, (2) to outline a method of constructing a simple form of deformation mechanism map, and (3) to present examples of maps for two representative oxides, a carbide, and three alkali halides.

2. Types of deformation mechanism maps

At the present time, there are two distinct types of deformation mechanism maps. The first type is of the form originally suggested by Weertman [1, 2], in which normalized stress is plotted against homologous temperature at constant grain size: the second type is of the form suggested by Mohamed and Langdon [3], in which normalized grain size is plotted against normalized stress at constant temperature. These two types are considered separately.

2.1. Deformation mechanism maps at constant grain size

Although developed predominantly for metals, maps of this type are now available for MgO [4, 5], olivine $[(Mg_{0.85}Fe_{0.15})_2SiO_4$–$(Mg_{0.95}Fe_{0.05})_2SiO_4]$ [5, 6], and UO_2 [4, 7].

An example is shown in Fig. 1 for polycrystalline MgO having a grain size of 10 μm, based on the work of Stocker and Ashby [5]. The temperature scale for this map extends from absolute zero to the melting point of MgO, and the scale of normalized shear stress, τ/G, extends over eight orders of magnitude, from 10^{-8} to 1, thereby including all stress–temperature conditions of interest in practical situations. The heavy lines on this map represent the boundaries between fields within which one specific deformation mechanism is dominant; the lines, therefore, trace out the loci of points where the two adjacent deformation mechanisms have equal strain-rates. These lines meet at triple junctions where three deformation mechanisms are of equal importance.

The upper line at $\tau/G \simeq 10^{-1}$ represents the ideal strength of MgO, based on the theoretical shear strength. The region marked dislocation glide represents conditions under which deformation occurs by the conservative motion of dislocations by glide through the lattice. Diffusion-controlled creep processes are rate-controlling at values of τ/G less than $\sim 5 \times 10^{-3}$, and this area is divided into high temperature (H.T.) and low temperature (L.T.) creep in which the gliding dislocation is released from an obstacle by climb, with the dominant transport mechanism occurring either through the lattice (H.T.) or along the dislocation cores (L.T.), respectively, and stress-directed diffusional creep. The area marked diffusional creep is further divided according to whether the diffusional process occurs by extrinsic O^{2-} lattice diffusion (Nabarro–Herring creep, $T/T_m > 0.42$), extrinsic O^{2-} grain-boundary diffusion (Coble creep, $0.17 < T/T_m < 0.42$), or intrinsic Mg^{2+} grain-boundary diffusion (Coble creep, $T/T_m < 0.17$).

The thin lines superimposed on the fields in Fig. 1 are contours of constant steady-state strain-rate, for rates from 10^{-2} to 10^{-10} sec^{-1}.* By selecting values of τ/G and T/T_m, this map, therefore, indicates both the approximate steady-state strain-rate and the dominant creep process for polycrystalline MgO having a grain size of 10 μm.

Fig. 1 also shows the location of experimental

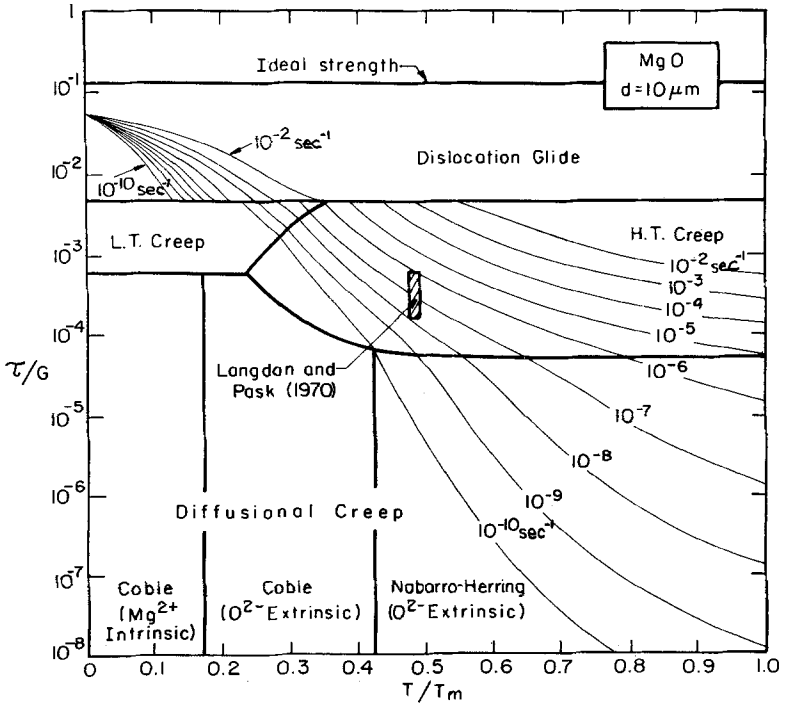

Figure 1 Deformation mechanism map for MgO having a grain size of 10 μm.

*Maps may also be constructed having contours of constant relaxation time, t_r, defined as the time required to produce a creep strain of σ/G, so that $t_r = \sigma/G\dot{e}$ where $\dot{e}$ is the steady-state creep rate [8].

data for MgO of a comparable grain size (11.8 μm) reported in an earlier creep investigation [9]; these results, which fall entirely within the field for high temperature creep, are discussed in more detail in Section 2.2.

2.2. Deformation mechanism maps at constant temperature

2.2.1. Constitutive equations for high temperature deformation

By considering a constant temperature, a deformation mechanism map may be constructed by plotting normalized grain size, d/b, against normalized stress, σ/G or τ/G, where d is the grain size and b is the Burgers vector [3]. Since the temperature is constant, this type of map may be regarded as a vertical section cut through a map at constant grain size (e.g. Fig. 1).

In order to develop these maps for ceramic materials, it is first of all necessary to determine the relevant constitutive equations for the deformation processes which may be important at the temperature of interest. At high temperatures, typically greater than $\sim 0.4\,T_m$, and for normalized stresses of σ/G less than $\sim 10^{-2}$,† Fig. 1 indicates that the dominant processes are high temperature creep and diffusional creep.

The processes of diffusional creep are well developed theoretically, and it is reasonable to use the existing theoretical equations.

When the diffusional path is through the lattice (Nabarro–Herring creep), the steady-state creep rate is given by [10, 11]

$$\dot{\epsilon} = \frac{B\Omega\sigma D_1}{d^2kT} \tag{1}$$

where B is a constant, Ω is the atomic volume, D_1 is the lattice diffusion coefficient, and k is Boltzmann's constant. The precise value of B depends on grain shape and load distribution, but a review of experimental data obtained on metals tested in tension suggests that $B \simeq 40$ [12], and this is consistent with a consideration of grain morphology in polycrystals [13]. Putting $\Omega = 0.7\,b^3$, Equation 1 reduces to

$$\dot{\epsilon} = 28\frac{D_1Gb}{kT}\left(\frac{b}{d}\right)^2\left(\frac{\sigma}{G}\right). \tag{2}$$

When the diffusional path is via the grain boundaries (Coble creep), the steady-state creep rate is given by [14]

$$\dot{\epsilon} = \frac{150\,\Omega\sigma\delta D_{gb}}{\pi d^3kT} \tag{3}$$

where δ is the effective width of the boundary for enhanced diffusivity, and D_{gb} is the grain-boundary diffusion coefficient. Taking $\delta = 2b$,‡ Equation 3 reduces to

$$\dot{\epsilon} = 66.8\frac{D_{gb}Gb}{kT}\left(\frac{b}{d}\right)^3\left(\frac{\sigma}{G}\right). \tag{4}$$

No single theory of high temperature creep is entirely satisfactory when an intragranular process is rate-controlling, but the constitutive equation may be derived directly from an analysis of the available experimental data. For an intragranular mechanism, the steady-state creep rate is independent of grain size and may be expressed as

$$\dot{\epsilon} = \frac{ADGb}{kT}\left(\frac{\sigma}{G}\right)^n \tag{5}$$

where D is the relevant diffusion coefficient, and A and n are constants. The values of these constants are, therefore, obtained by logarithmically plotting the normalized creep rate, $\dot{\epsilon}kT/DGb$, against the normalized stress, σ/G.

Fig. 2 shows published creep data for three materials, Al_2O_3 [15], MgO [9], and UC [16]. These results were selected because the experiments are documented in detail, and the tests on each material were conducted in compression so that there are no problems associated with the interpretation of bending data. For each material, the diffusion coefficient was taken for lattice diffusion of the slower-moving ion, and the shear modulus at a selected absolute temperature, T, was estimated from the relationship

$$G = G_0 - (\Delta G)T \tag{6}$$

†Owing to the rapid strain-rates involved at high temperatures, a value of $\sigma/G \sim 10^{-2}$ represents an upper limit of interest for most practical and experimental conditions.

‡There is evidence that the value of δ in many ceramic materials may be larger than $2b$, due both to a space-charge effect and to impurity segregation at or in the vicinity of the boundaries. In the absence of definitive data on this point, it is usual to put $\delta = 2b$ and to recognize that this may be regarded as a lower limit. A similar approximation was used in the construction of Fig. 1.

TABLE I Values of D, G, and b for various ceramic materials

Material	D(cm^2 sec^{-1})	G			References	
		G_0(MN m^{-2})	ΔG(MN m^{-2} K^{-1})	b(cm)	D	G
Al_2O_3	$D_l(O^{2-}) = 2.0 \exp(-461\,000/RT)$*	1.71×10^5	23.4	4.75×10^{-8}†	[17]	[18]
MgO	$D_l(O^{2-}) = 2.5 \times 10^{-6} \exp(-261\,000/RT)$	1.387×10^5	26.2	2.98×10^{-8}	[19]	[20]
UC	$D_l(U^{4+}) = 7.5 \times 10^{-5} \exp(-339\,000/RT)$	2.058×10^6	16.1	3.51×10^{-8}	[21]	[22]
KCl	$D_l(Cl^-) = 3.2 \exp(-189\,000/RT)$	1.225×10^4	6.57	4.45×10^{-8}	‡	[24]
LiF	$D_l(F^-) = 64 \exp(-212\,000/RT)$	5.52×10^4	33.2	2.85×10^{-8}	[25]	[24]
NaCl	$D_l(Cl^-) = 2.2 \times 10^2 \exp(-214\,000/RT)$	1.79×10^4	9.6	3.99×10^{-8}	‡	[24]

*$R = 8.31$ J mol^{-1} K^{-1}.
† For slip on $\{0\,0\,0\,1\}\langle 1\,1\,\bar{2}\,0\rangle$ basal system.
‡Value of D_l estimated for the appropriate grain size from Laurent and Bénard [23].

where G_0 is the value of G obtained by a linear extrapolation from high temperatures to absolute zero and ΔG is the variation in G per degree Kelvin. The values of D, G_0, ΔG, and b are summarized in the first three lines of Table I, where R is the gas constant and the activation energies are in J mol^{-1}.

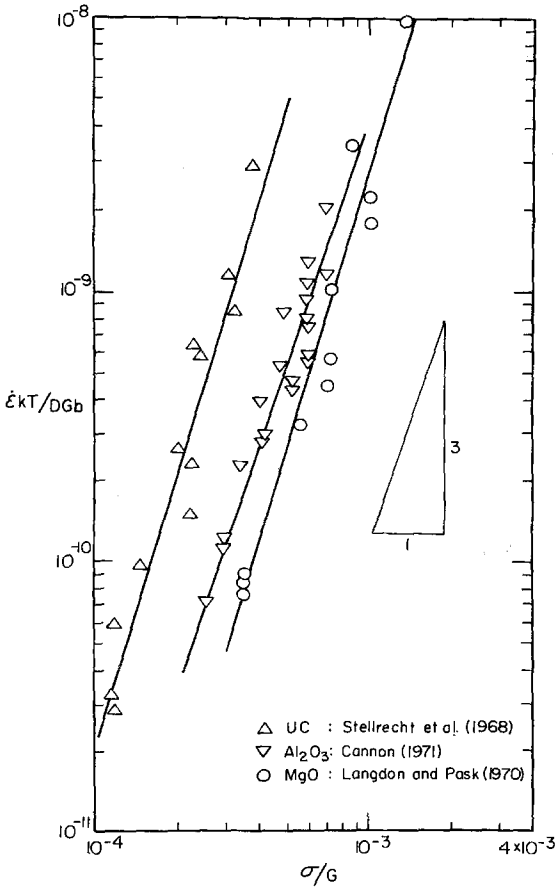

Figure 2 Normalized creep rate, $\dot{\epsilon}kT/DGb$, versus normalized stress, σ/G, for Al_2O_3, MgO, and UC.

As indicated in Fig. 2, the results for Al_2O_3 and MgO are in excellent agreement, and the experimental lines differ by only a factor of two. This provides strong support for the form of Equation 5 when it is noted that there are major differences between these two materials in both testing temperature (1600, 1650 and 1700° C for Al_2O_3, and 1200° C for MgO) and grain size (65 μm for Al_2O_3, and 11.8, 33 and 52 μm for MgO). The results for UC are about an order of magnitude higher, and this may be due to uncertainties in the value of $D_l(U^{4+})$.

The data in Fig. 2 indicate a stress exponent of $n \sim 3$, so that the constitutive equation for dislocation creep* in ceramic oxides and carbides may be expressed by the relationship

$$\dot{\epsilon} = 3\frac{D_l G b}{kT}\left(\frac{\sigma}{G}\right)^3 \qquad (7)$$

where the value of $A \sim 3$ is obtained from a best fit to the results for Al_2O_3 and MgO.†

2.2.2. Method of constructing a deformation mechanism map

The method of constructing a deformation mechanism map at constant temperature is illustrated in Fig. 3 for MgO at 1200° C. In this map, the range of normalized grain size, d/b, is from 10^3 to 10^8, corresponding to grain sizes from a minimum of $\sim 0.3\,\mu$m to a maximum of ~ 3 cm, and the range of normalized stress, σ/G, is from 10^{-7} to 10^{-2}. At this temperature, laboratory experiments are generally conducted in the range of $\sigma/G \sim 10^{-4}$ to 10^{-3} but structural applications are usually in the range of $\sigma/G \sim 10^{-6}$ to 10^{-4}.

The map is constructed using three constitutive

*The term dislocation creep is used to designate the deformation mechanism at high stress levels when there is no dependence on grain size: the precise nature of this process is not known at the present time.

†In the construction of Fig. 1, Equation 5 was used with $A = 11.6$ and $n = 3.3$ [4, 5].

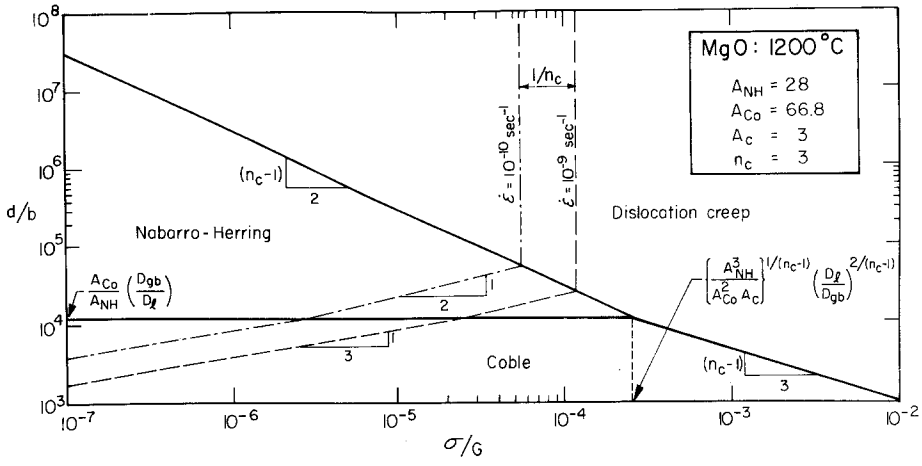

Figure 3 Method of constructing a deformation mechanism map, illustrated for MgO at 1200° C.

relationships, given by Equation 7 for dislocation creep, Equation 2 for Nabarro–Herring creep, and Equation 4 for Coble creep: the insert in Fig. 3 summarizes the values of the dimensionless constant A in the Nabarro–Herring (A_{NH}), Coble (A_{Co}), and dislocation creep (A_c) equations, and the stress exponent used for dislocation creep (n_c). The map is constructed following a simple three-step procedure.

(1) From Equations 2 and 4, the boundary between the Nabarro–Herring and Coble mechanisms is defined as

$$\frac{d}{b} = \frac{A_{Co}}{A_{NH}}\left(\frac{D_{gb}}{D_l}\right) \tag{8}$$

where D_{gb} and D_l are the values of the diffusion coefficients calculated for a temperature of 1200° C. Very little definitive information is available on the rates of grain-boundary diffusion in ceramics, so that D_{gb} was calculated by taking $Q_{gb} = 0.6\,Q_l$, where Q_{gb} and Q_l are the activation energies for grain-boundary and lattice diffusion, respectively, and $D_{0(gb)} = D_{0(l)}$, where D_0 is the value of the pre-exponential frequency factor in the diffusion relationship.‡ Since Nabarro–Herring and Coble creep both exhibit the same dependence on stress ($n = 1$), the Nabarro–Herring/Coble boundary is obtained by drawing a horizontal line through the value of d/b given by Equation 8: this line is shown in Fig. 3.

(2) The Nabarro–Herring/Coble boundary terminates at a triple point where the three deformation mechanisms have equal strain-rates. From Equations 2, 4 and 7, the value of the normalized stress at this point is given by

$$\frac{\sigma}{G} = \left(\frac{A_{NH}^3}{A_{Co}^2 A_c}\right)^{1/(n_c-1)}\left(\frac{D_l}{D_{gb}}\right)^{2/(n_c-1)}. \tag{9}$$

Equation 9, therefore, indicates the upper limit of normalized stress for the Nabarro–Herring/Coble boundary.

(3) The slope of the boundary separating any two mechanisms is given by

$$\text{slope} = \frac{\Delta n}{\Delta p} \tag{10}$$

where Δn and Δp are the differences in the exponents for stress and inverse grain size, respectively, for the two mechanisms on either side of the line. The slopes of the Nabarro–Herring/dislocation creep and Coble/dislocation creep boundaries are, therefore, $-(n_c - 1)/2$ and $-(n_c - 1)/3$, respectively: for $n_c = 3$, these slopes are equivalent to -1 for the Nabarro–Herring/dislocation creep boundary and $-2/3$ for the Coble/dislocation creep boundary. Lines having these slopes are drawn in Fig. 3 from the point on the Nabarro–Herring/Coble boundary given by Equation 9.

The map is now complete for MgO at 1200° C.

2.2.3. Method of inserting contours of constant strain rate

Three steps are required in order to insert con-

‡It should be noted that there are invariably slight differences in the values assumed for D_{gb} by different investigators. For example, the present work takes $Q_{gb} = 0.6\,Q_l$, which is equivalent to $Q_{gb} = 157\,\text{kJ mol}^{-1}$ for O^{2-} diffusion, whereas Stocker and Ashby [5] assumed a value of $Q_{gb} = 173\,\text{kJ mol}^{-1}$ in the construction of Fig. 1: both analyses assume that $D_{0(gb)} = D_{0(l)}$.

tours of constant strain-rate.

(1) It is necessary to solve one of the constitutive equations at a point within one of the established fields. For example, Equation 5 may be expressed as

$$\frac{\sigma}{G} = \left(\frac{\dot{\epsilon}kT}{ADGb}\right)^{1/n}. \quad (11)$$

Since dislocation creep is independent of grain size, the position of the strain-rate contour corresponding to $\dot{\epsilon} = 10^{-10}\text{sec}^{-1}$ may be obtained by solving Equation 11 and drawing a vertical line within the dislocation creep field at the relevant value of σ/G. This line is shown in Fig. 3.

(2) The slope of the constant strain rate contour within any field is given by

$$\text{slope} = \frac{n}{p} \quad (12)$$

where n and p are the exponents of stress and inverse grain size, respectively, for the two mechanisms appropriate to the field. This is equivalent to slopes of $\frac{1}{2}$ for Nabarro–Herring creep and $\frac{1}{3}$ for Coble creep. The contour for $\dot{\epsilon} = 10^{-10}\text{sec}^{-1}$ may, therefore, be continued into other fields by drawing lines having the appropriate slopes from the points of intersection at the boundaries. This construction is indicated in Fig. 3.

(3) Additional contours may be added for other strain-rates, since an order of magnitude change in $\dot{\epsilon}$ displaces the contour by a factor of $1/n$ when measured parallel to the stress axis. The contour for $\dot{\epsilon} = 10^{-9}\text{sec}^{-1}$ shown in Fig. 3 is, therefore, displaced by a factor of $1/n_c$ from the line for 10^{-10}sec^{-1} within the field for dislocation creep. Using this procedure, it is, therefore, very easy to insert on to the map those constant strain-rate contours which are of maximum interest. The strain-rates of 10^{-10} and 10^{-9}sec^{-1} were selected for illustrative purposes in this work because 10^{-9}sec^{-1}, corresponding to a strain of slightly less than 0.01%/day, represents essentially a lower limit for laboratory experiments, whereas 10^{-10} sec^{-1}, corresponding to a strain of ~ 3%/10 years, represents an upper limit for many structural design criteria.

The final form of the deformation mechanism map is shown in Fig. 4. This is identical to the map illustrated schematically in Fig. 3, with the exception that the strain-rate contours are curved in the vicinity of the boundaries between two adjacent fields. This curvature arises because the contours in Fig. 4 were calculated by computer, and therefore all mechanisms were considered at every point in grain size-stress space. In principle, the procedure of drawing straight lines up to the boundaries is an oversimplification, because it ignores the contributions from mechanisms in adjacent fields; in practice, however, this additional contribution is only significant in the immediate vicinity of the boundaries, and for most situations the procedure is acceptable.*

Fig. 4 also indicates the range of stress and grain size used for the MgO creep data in Fig. 2: these data are identical to that recorded in Fig. 1.

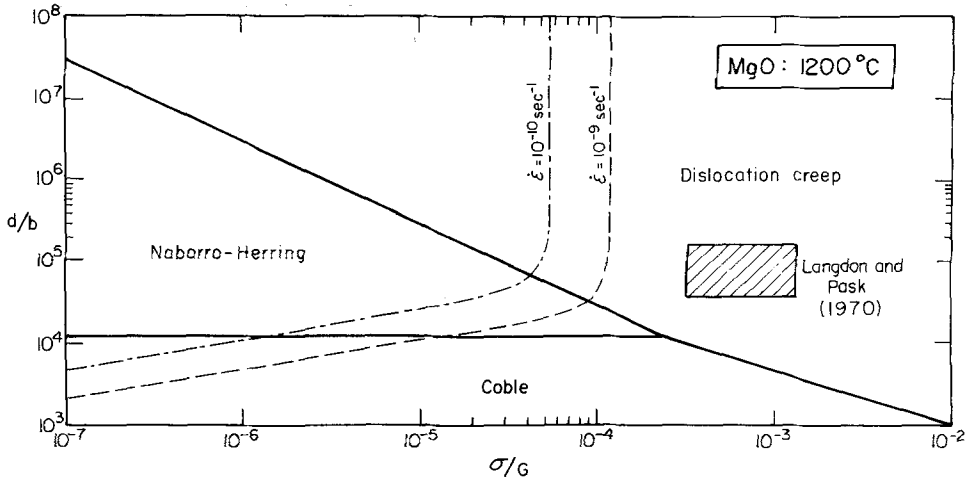

Figure 4 Deformation mechanism map for MgO at 1200° C.

*The maximum error introduced by drawing strain-rate contours as straight lines occurs at a triple point, where the strain rate is underestimated by a factor of three: this is invariably smaller than the errors inherent in the constitutive equations used to construct the map.

3. Deformation mechanism maps for other ceramics

3.1. Oxides and carbides

It is apparent from Fig. 2 that the dislocation creep mechanism in Al_2O_3 and UC may also be represented by a relationship of the form shown in Equation 7. Deformation mechanism maps were, therefore, constructed for these two materials using the procedure outlined in Section 2.2, with the exception that the constant strain-rate contours were calculated by computer.

The results are shown in Figs. 5 and 6 for Al_2O_3 at 1650° C and UC at 1300° C, respectively. These maps also indicate the location of the experimental data in grain size-stress space,† and the positions of the constant strain-rate contours for 10^{-9} and 10^{-10} sec^{-1}.

3.2. Alkali halides

A recent analysis of creep behaviour in three alkali halides indicated that the stress exponent in these materials was close to 5 [26]. This is confirmed by the data plotted in Fig. 7, using experimental results reported for NaCl [27], KCl [28], and LiF [29]. As before, all experiments were conducted in compression, the diffusion coefficient was put equal to the measured value for lattice diffusion of the slower-moving ion, and the shear modulus was estimated from Equation 6: the relevant values of D, G_0, ΔG, and b are shown in Table I.

These three sets of results are in excellent agreement over five orders of magnitude of normalized strain-rate, despite large differences in testing temperature (365 to 742° C for NaCl, 600° C for KCl, 400 to 550° C for LiF) and grain size (~ 200 to 3000 μm for NaCl, in the range of 100 to 300 μm for KCl, 160 to 3000 μm for LiF). The results, therefore, suggest that the dislocation creep process for these alkali halides may be expressed by the relationship

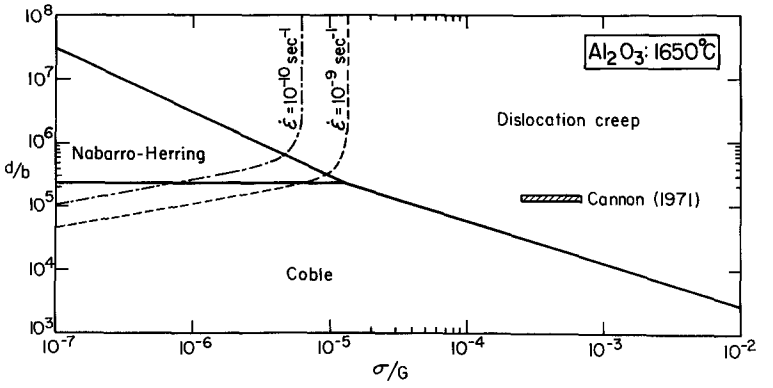

Figure 5 Deformation mechanism map for Al_2O_3 at 1650° C.

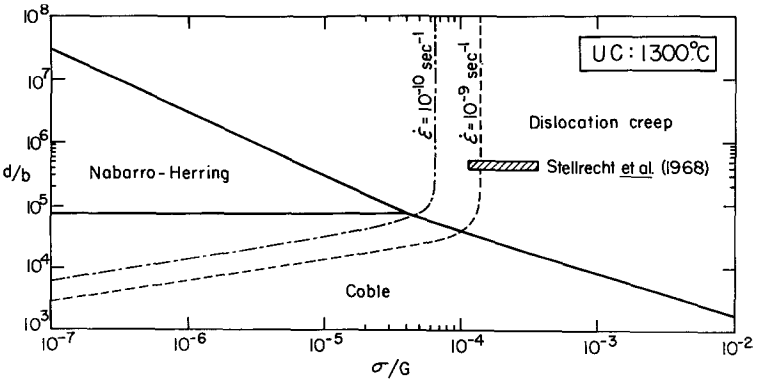

Figure 6 Deformation mechanism map for UC at 1300° C.

†In the compressive creep experiments on UC, the grain size of the material was not quoted: an examination of the photomicrographs [16] suggests $d \simeq 160 \pm 15$ μm.

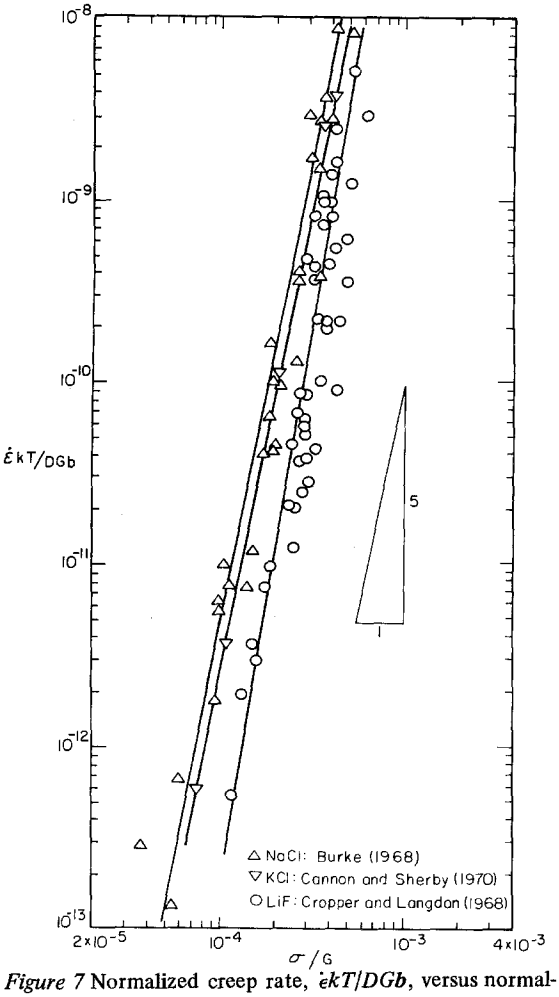

Figure 7 Normalized creep rate, $\dot{\epsilon}kT/DGb$, versus normalized stress, σ/G, for KCl, LiF, and NaCl.

$$\dot{\epsilon} = 3 \times 10^8 \frac{D_1 Gb}{kT}\left(\frac{\sigma}{G}\right)^5 \qquad (13)‡$$

Using Equations 2, 4 and 13, deformation mechanism maps were constructed for NaCl at 600° C, KCl at 600° C, and LiF at 500° C: the results are shown in Figs. 8, 9 and 10, respectively, and these maps also indicate the location of the experimental data used in the construction of Fig. 7.

4. The superimposition of deformation mechanism maps

Deformation mechanism maps may be superimposed for different materials provided only three mechanisms are considered and the same set of constitutive equations describes the deformation processes in all materials. For example, the deformation mechanism maps for MgO, Al_2O_3, and UC are identical in form, although the triple point where the three mechanisms are of equal importance occurs at a different position on each map because there has been no normalization for temperature. Similarly, the maps for NaCl, KCl, and LiF are also similar in appearance.

A set of similar maps may be superimposed by compensating for differences in temperature: reference to Fig. 3 indicates that this is achieved by plotting $(d/b)(D_1/D_{gb})$ versus $(\sigma/G)(D_{gb}/D_1)^{2/(n_c-1)}$.

An example of this type of map is shown in Fig. 11 for the two oxides and UC. The position of the triple point is defined on the normalized grain size axis by

$$\frac{A_{Co}}{A_{NH}} = 2.385 \qquad (14)$$

and on the normalized stress axis by

$$\left(\frac{A_{NH}^3}{A_{Co}^2 A_c}\right)^{1/(n_c-1)} = 1.28. \qquad (15)$$

The locations of the experimental data for these three materials are also indicated on the map.

5. Discussion

Deformation mechanism maps present a simple and highly visual method of displaying information on the mechanical properties of materials. It seems likely that this type of mapping will become increasingly important as more information is obtained on the nature of the constitutive equations for different deformation mechanisms under specific experimental conditions: indeed, deformation mechanism maps have already been likened to phase diagrams [33].

Of the two types of maps discussed in Section 2, the maps at constant temperature have the major advantage of considerable simplicity in construction. Whereas maps at constant grain size are constructed by computer, by solving the relevant constitutive equations at a very large number (~ 6000) of points in stress-temperature space, maps at constant temperature may be constructed

‡The reason for the larger value of n in the alkali halides is not known at the present time. It has been suggested that the ratio of the anion to cation radius may be important [30], such that ratios greater than 2 give $n \sim 3$ and ratios less than 2 give $n \sim 5$, or that it may arise due to differences in the nature of the atomic bonds [31]. An alternative possibility is that $n \sim 5$ behaviour represents a dislocation climb process whereas $n \sim 3$ behaviour arises when dislocation glide is rate-controlling, in a manner analogous to the climb and glide observed in metallic solid solution alloys [32].

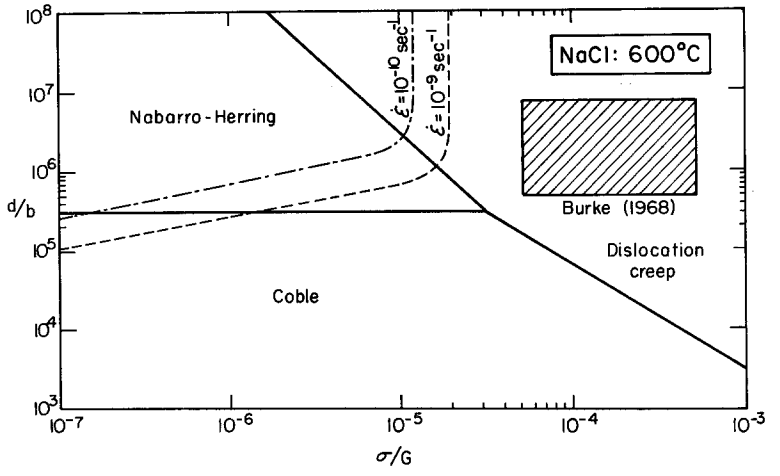

Figure 8 Deformation mechanism map for NaCl at 600° C.

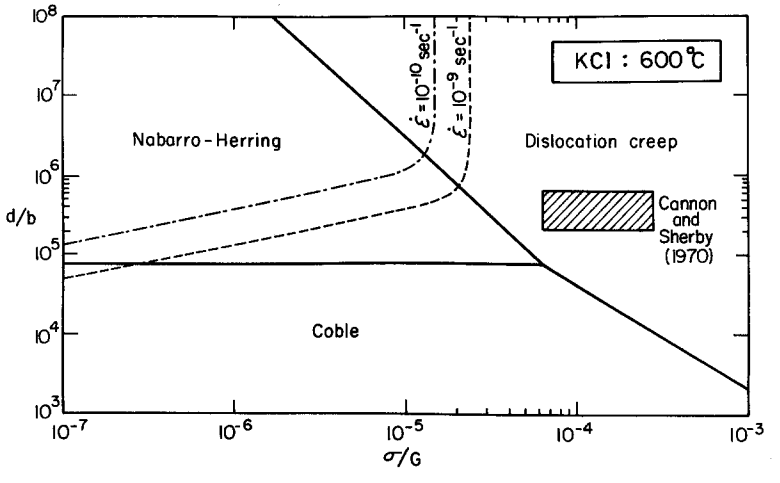

Figure 9 Deformation mechanism map for KCl at 600° C.

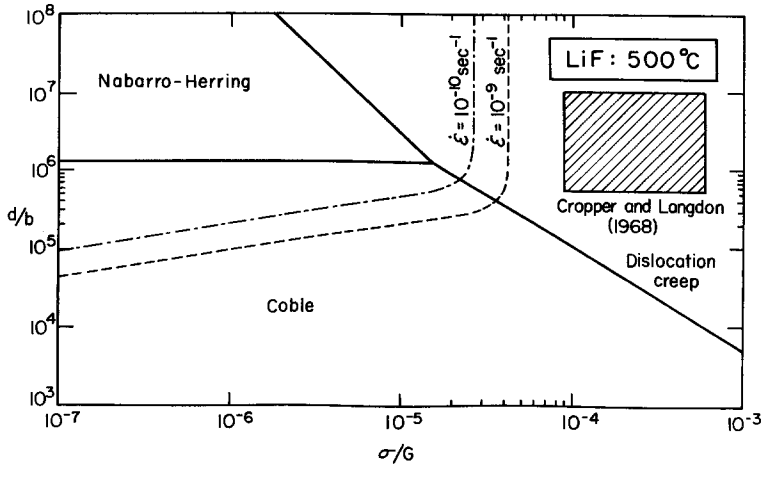

Figure 10 Deformation mechanism map for LiF at 500° C.

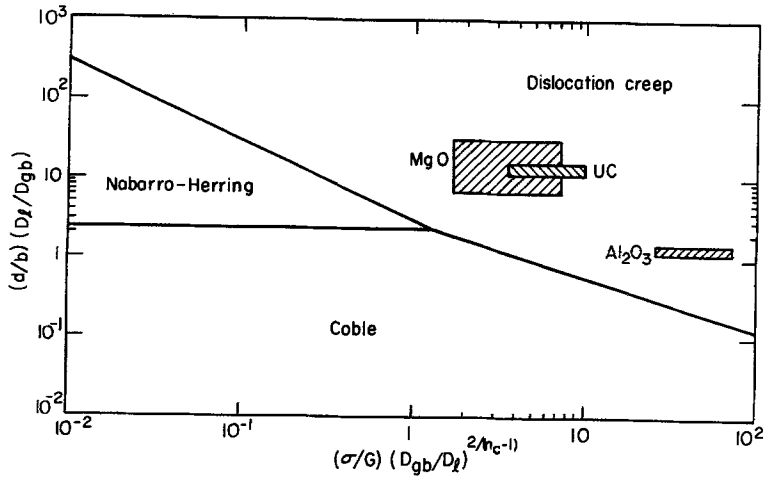

Figure 11 Method of superimposing a set of similar deformation mechanism maps, illustrated for Al_2O_3, MgO, and UC.

very easily, even when more than three mechanisms are operative, using the procedure depicted schematically in Fig. 3 and outlined in detail in Section 2.2.

There are two major advantages of constructing maps at constant temperature. Firstly, provided the individual mechanisms operate independently so that the strain-rates are additive, the various fields are separated by straight rather than curved boundaries.* Secondly, engineering applications usually relate to a fairly narrow range of temperature, so that grain size and stress are often the permissible variables: the maps at constant temperature are, therefore, ideal for many practical situations.

It is important to emphasize two limitations associated with both types of deformation mechanism maps: (1) the accuracy of the map is limited by the accuracy of the constitutive equations, and this is of particular importance with ceramic materials because of the uncertainties in the values of the diffusion coefficients; (2) some mechanisms are probably excluded from the present maps, even though they may be of major importance under certain experimental conditions, because of the lack of information on the relevant constitutive equations. Provided these limitations are not overlooked, deformation mechanism maps present a visual summary of available mechanical data and, used judiciously, are valuable in the prediction of creep behaviour.

6. Summary and conclusions

(1) Deformation mechanism maps may be constructed at either constant grain size or constant temperature.

(2) A simple method is presented for constructing maps at constant temperature, and for inserting constant strain-rate contours.

(3) Examples of maps are presented for two oxides, a carbide, and three alkali halides.

(4) A method is described for superimposing a set of similar deformation mechanism maps.

Acknowledgement

This work was supported by the United States Energy Research and Development Administration under Contract E(04–3)–113 PA–26.

References

1. J. WEERTMAN and J. R. WEERTMAN, "Physical Metallurgy", edited by R. W. Cahn (North-Holland, Amsterdam, 1965) p. 793.
2. J. WEERTMAN, *Trans. Amer. Soc. Metals* **61** (1968) 681.
3. F. A. MOHAMED and T. G. LANGDON, *Met. Trans.* **5** (1974) 2339.
4. M. F. ASHBY, *Acta Met.* **20** (1972) 887.
5. R. L. STOCKER and M. F. ASHBY, *Rev. Geophys. Space Phys.* **11** (1973) 391.
6. J. WEERTMAN and J. R. WEERTMAN, *Ann. Rev. Earth and Planetary Sci.* **3** (1975) 293.
7. J. T. A. ROBERTS and J. C. VOGLEWEDE, *J. Amer. Ceram. Soc.* **56** (1973) 472.
8. J. H. GITTUS, *Phil. Mag.* **30** (1974) 751.
9. T. G. LANGDON and J. A. PASK, *Acta. Met.* **18** (1970) 505.
10. F. R. N. NABARRO, "Report of a Conference on Strength of Solids" (The Physical Society, London, 1948) p. 75.
11. C. HERRING, *J. Appl. Phys.* **21** (1950) 437.
12. J. E. HARRIS, *Met. Sci. J.* **7** (1973) 1.
13. R. C. GIFKINS, T. G. LANGDON and D. McLEAN, *Met. Sci.* **9** (1975) 141.

*A method of constructing maps for sequential mechanisms is described elsewhere [34].

14. R. L. COBLE, *J. Appl. Phys.* **34** (1963) 1679.
15. W. R. CANNON, Ph.D. thesis, Department of Materials Science, Stanford University (1971).
16. D. E. STELLRECHT, M. S. FARKAS and D. P. MOAK, *J. Amer. Ceram. Soc.* **51** (1968) 455.
17. Y. OISHI and W. D. KINGERY, *J. Chem. Phys.* **33** (1960) 480.
18. D. H. CHUNG and G. SIMMONS, *J. Appl. Phys.* **39** (1968) 5316.
19. Y. OISHI and W. D. KINGERY, *J. Chem. Phys.* **33** (1960) 905.
20. N. SOGA and O. L. ANDERSON, *J. Amer. Ceram. Soc.* **49** (1966) 355.
21. P. VILLAINE, *Diffusion Data* **3** (1968) 515.
22. A. PADEL and CH. DE NOVIAN, *J. Nuclear Mater.* **33** (1969) 40.
23. J. F. LAURENT and J. BÉNARD, *J. Phys. Chem. Solids* **7** (1958) 218.
24. S. HART, *J. Phys. D* **1** (1968) 1285.
25. M. EISENSTADT, *Phys. Rev.* **132** (1963) 630; HJ. MATZKE, *J. Phys. Chem. Solids* **32** (1971) 437.
26. F. A. MOHAMED and T. G. LANGDON, *J. Appl. Phys.* **45** (1974) 1965.
27. P. M. BURKE, Ph.D. thesis, Department of Materials Science, Stanford University (1968).
28. W. R. CANNON and O. D. SHERBY, *J. Amer. Ceram. Soc.* **53** (1970) 346.
29. D. R. CROPPER and T. G. LANGDON, *Phil. Mag.* **18** (1968) 1181.
30. W. R. CANNON and O. D. SHERBY, *J. Amer. Ceram. Soc.* **56** (1973) 157.
31. S. H. KIRBY and C. B. RALEIGH, *Tectonophysics* **19** (1973) 165.
32. F. A. MOHAMED and T. G. LANGDON, *Acta Met.* **22** (1974) 779.
33. G. R. TERWILLIGER and K. C. RADFORD, *Bull. Amer. Ceram. Soc.* **53** (1974) 172.
34. F. A. MOHAMED and T. G. LANGDON, *Scripta Met.* **9** (1975) 137.

Received 16 June and accepted 7 July 1975.